

Experimental Demonstration of a Quantum-Optimal Coronagraph Using Spatial Mode Sorters

Nico Deshler,^{1,*} Itay Ozer,^{2,*} Amit Ashok,¹ and Saikat Guha²

¹Wyant College of Optical Sciences, University of Arizona, Tucson, AZ 85721, USA

²Department of Electrical and Computer Engineering,
University of Maryland, College Park, MD 20742, USA

(Dated: July 18, 2024)

An ideal direct imaging coronagraph, which selectively rejects the fundamental mode of a telescope, has been shown to achieve the quantum information limits for exoplanet detection and localization. In this study, we experimentally implement this quantum-optimal coronagraph using spatial mode (de)multiplexing. Our benchtop system includes a forward and inverse pass through a free-space programmable spatial mode sorter, designed to isolate photons in a point spread function (PSF)-adapted basis. During the forward pass, the fundamental mode is rejected, effectively eliminating light from an on-axis point-like star. On the inverse pass, the remaining modes are coherently recombined, enabling direct imaging of a faint companion. We develop a probabilistic measurement model that accounts for combined effects of fundamental shot noise and experimental noise specific to our benchtop setup, such as modal cross-talk, dark noise, and ambient background illumination. We leverage this measurement model to formulate a maximum-likelihood estimator of the exoplanet position given an image captured with the coronagraph. Using this approach, we successfully localize an artificial exoplanet at sub-diffraction distances ($< \sigma$) from its host star under a 1000:1 star-planet contrast ratio. Our system accurately localizes the exoplanet up to an absolute error $< 0.03\sigma$ over the separation range $[0, 0.6]\sigma$. Finally, we numerically evaluate the precision of our experimental coronagraph against state-of-the-art coronagraphs subject to comparable noise models.

I. INTRODUCTION

The challenge of discovering habitable planets beyond our solar system has motivated astronomers to develop a diverse repertoire of exoplanet detection techniques. Broadly speaking, transit photometry, radial velocity, gravitational microlensing, and astrometry methods all monitor perturbations to the brightness, position, and spectrum of a prospective host star over time to infer the presence and dynamics of a faint orbiting companion [1]. While these methods have enjoyed great success in detecting exoplanets, contributing over 5,500 confirmed discoveries to date [2, 3], they fundamentally rely on *indirect* observations which provide limited information about more detailed planetary features. Remotely characterizing atmospheric composition, weather patterns, surface temperature, and surface gravity is crucial for understanding extrasolar chemical environments and identifying potential biosignatures [4, 5].

By comparison, direct imaging techniques aspire to spatially observe/resolve orbiting exoplanets, providing more comprehensive planetary data [6, 7]. However, direct imaging faces two compounding phenomenological challenges. First, exoplanets are extremely faint compared to their host stars, with relative brightness factors ranging from 10^{-5} for Hot Jupiters to 10^{-11} for Exo-Earths in the habitable zone. Second, the distance between an exoplanet and its host star often falls below the optical resolution capabilities of current space-based telescopes, residing in the so-called 'sub-diffraction regime' [8]. When imaged with a conventional telescope,

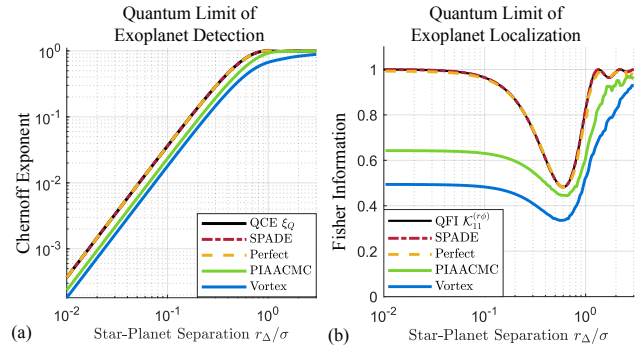


FIG. 1. Comparisons between the Chernoff exponent (a) and the Fisher information per photon (b) for various coronagraph designs relative to the quantum limits (black) of exoplanet detection and localization at high contrasts. The Perfect Coronagraph (dashed yellow) is the focus of this work and is shown to theoretically saturate both quantum limits in [17]. State-of-the-art systems such as the phase-induced amplitude apodization complex mask coronagraph (PIAACMC) [11] and the vortex coronagraph [9] are notably sub-optimal in the sub-diffraction regime.

light from the exoplanet overlaps with prominent diffraction features of the host star. This overlap, combined with the overwhelming shot noise generated by the bright star, effectively renders the exoplanet undetectable. Developments in coronagraph techniques have enabled complete nulling of an on-axis point-like star so that, in the absence of ambient background illumination, only light from the exoplanet reaches the detector [9–14]. In this way, state-of-the-art coronagraphs suppress photon shot noise intrinsic to measurements of classical states of light, thereby enhancing the signal-to-noise ratio of exoplanet signatures [15, 16].

* Authors contributed equally to this work.

Inspired by new insights in passive superresolution imaging [18–21], we recently reported the quantum information limits for exoplanet detection and localization [17]. Our findings revealed that these limits are achieved by a direct-imaging coronagraph that exclusively rejects the fundamental mode of the telescope. In contrast, current state-of-the-art coronagraphs discard information-bearing photons in higher-order modes [22], resulting in sub-optimal performance over the sub-diffraction regime, as illustrated in Figure 1. Quantum-optimal coronagraphs, however, preserve information at sub-diffraction star-planet separations, where an abundance of exoplanets are expected to reside, given current statistical models [23–26].

In this work, we propose a quantum-optimal direct imaging coronagraph using a spatial mode sorter implemented with a multi-plane light converter (MPLC) [27–29]. To the best of our knowledge, this is the first experimental verification of a coronagraph design that theoretically saturates the quantum limits for exoplanet discovery tasks. Applying a maximum likelihood estimator to images collected with our bench-top setup, we localize an artificial exoplanet at sub-diffraction separations from an artificial host star with a contrast ratio of 1000:1. Denoting the Rayleigh diffraction limit of our imaging system as σ , the absolute error of the empirical mean MLE remains below 0.03σ over the separation range $[0, 0.6]\sigma$. The empirical precision (standard deviation) of the MLE varies over the sub-diffraction regime between $\sim 0.1\sigma$ and $\sim 0.01\sigma$ for an exoplanet in the range $[0, 0.1]\sigma$ and $[0.1, 0.6]\sigma$, respectively. We invoke a probabilistic measurement model to characterize the impact of real-world noise sources and experimental constraints expected in an operating environment which hinder the attainment of quantum-limited performance set by shot noise.

II. METHODS

A. Experimental Design

Figure 2(a) illustrates the working principles of a quantum-optimal coronagraph design based on two cascaded mode sorters. The first mode sorter decomposes the incident optical field into a PSF-adapted transverse spatial mode basis [30] in order to isolate and eliminate photons in the fundamental mode. The second sorter inverts the mode decomposition, coherently recombining light in the residual modes to form an image of the exoplanet on a detector array. This scheme can be viewed as spatial mode filtering.

Our experimental setup shown in Figure 2b emulates these working principles by double-passing the optical field through a single mode sorter implemented on a 3-plane MPLC [31]. On the forward pass, the MPLC spatially demultiplexes the optical field in the Fourier-Zernike modes (Appendix A), which constitute a PSF-adapted basis for circular apertures, and focuses light in each mode to a distinct Gaussian spot on the sorting plane. The spot corresponding to the funda-

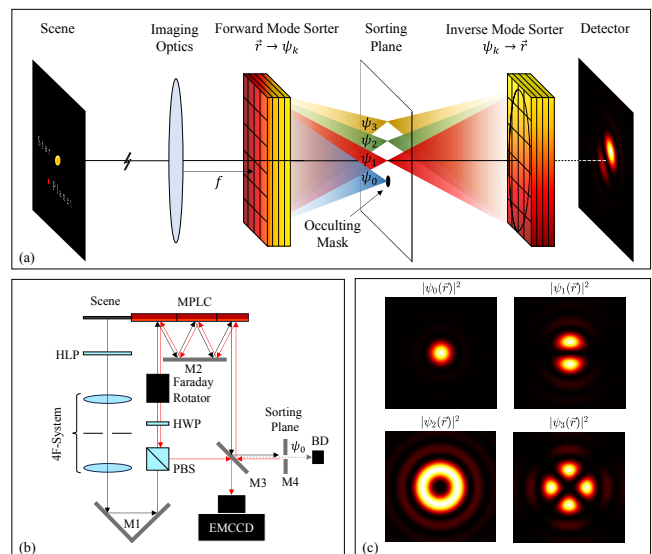


FIG. 2. (a) Conceptual design of a quantum-optimal direct-imaging coronagraph based on spatial mode sorting. The forward mode sorter demultiplexes the field incident on the image plane into a PSF-adapted basis. Light in the fundamental mode is rejected by a mask at the sorting plane while light in the remaining modes propagates freely to an inverse mode sorter. The inverse mode sorter coherently recombines the light to form an image at the detector. (b) Schematic of the experimental implementation of a quantum-optimal coronagraph using an MPLC mode sorter and non-reciprocal polarization elements. (c) Intensity profiles of the truncated Fourier-Zernike mode basis used in our experiment.

mental mode is directed to the opening of a pinhole mirror and absorbed at a beam dump. The remaining modes reflect off the pinhole mirror and are sent backwards through the mode sorter. The unitary nature of spatial mode sorting inverts the mode transformation during the backward pass. Non-reciprocal polarization elements split the optical path for the forward (pre-nulling) and backward (post-nulling) pass, sending the filtered field to a detector. Through this process, the field at the detector plane is identical to the field at the focal plane minus optical contribution from the fundamental mode. The $4f$ imaging system used in our setup is characterized by a circular aperture diameter $D = 400\mu\text{m}$ and a focal length $f = 200\text{mm}$ operating at wavelength $\lambda = 532\text{nm}$, yielding a Rayleigh resolution of $\sigma = 1.22\lambda f/D = 324\mu\text{m}$ on the object plane.

We prioritize demonstrating exoplanet localization at sub-Rayleigh star-planet separations; the regime where quantum-optimal coronagraphs offer the greatest theoretical advantage over existing high-performance coronagraph designs. To sample this separation regime, we align the coronagraph to a bright on-axis point-source (artificial star) and vertically step the position of a second dim point-source (artificial exoplanet) $\vec{r}_e = (0, y_e)$ over the discrete domain $y_e \in \mathcal{Y} = [-a : \Delta : +a]$ with endpoints $a = .85\sigma$ and sampling step size $\Delta = .0215\sigma$.

Light from a sub-diffraction exoplanet couples predominantly to lower-order Fourier-Zernike modes. We

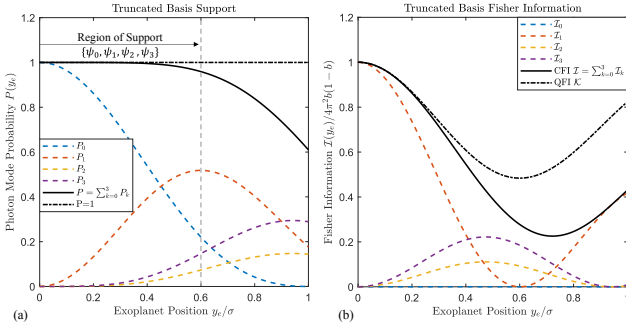


FIG. 3. (a) Theoretical mode detection probabilities as a function of off-axis source location for the truncated set of Fourier-Zernike modes. The nominal 'region of support' is given by off-axis positions in the domain $[0, 0.6]\sigma$ within which $> 95\%$ of the light energy couples to the truncated mode basis. (b) Distribution of the classical Fisher information in each mode as a function of off-axis position. The classical Fisher information of the truncated mode basis remains within 10% of the quantum Fisher information limit over the domain $\sim [0, 0.4]\sigma$. Outside this domain, the information concentrates in higher-order modes that are ignored by our mode-sorter.

therefore configured the MPLC to sort a truncated basis $\{\psi_0(\vec{r}), \psi_1(\vec{r}), \psi_2(\vec{r}), \psi_3(\vec{r})\}$ where $\psi_0(\vec{r})$ is the fundamental mode of the imaging system (Figure 2c). Collectively, these modes contain a majority of the energy in the field generated by a sub-Rayleigh companion as shown in Figure 3. We define the nominal region of support for this truncated basis to be $|y_e| \leq .6\sigma$. Expanding the basis to more than four modes was found to significantly degrade the cross-talk of the mode sorter due to the limited number of phase masks available on our programmable MPLC. In principle, introducing more masks would allow one to sort more modes and temper modal cross-talk, enabling access to greater star-planet separations and contrasts.

B. Measurement Model

We invoke a theoretically and empirically-driven probability distribution for the direct imaging measurement. Let $\mathbf{X}(\vec{r}_0) \in \mathbb{R}^M$ be a random vector containing the number of photons measured at each pixel of the detector over fixed exposure time T when imaging a single point-source located at position \vec{r}_0 . The number of photons measured in each pixel are independent and modeled with Poisson statistics,

$$\mathbf{X}(\vec{r}_0) \sim \text{Pois}(\lambda_0 \mathbf{q}(\vec{r}_0) + \lambda_B \mathbf{p}_B) \quad (1)$$

where $\lambda_0 \in \mathbb{R}$ is the photon flux entering the pupil from the point source, $\mathbf{q}(\vec{r}_0) \in \mathbb{R}^M$ is the post-nulling photon arrival probability at each detector pixel after propagating the pupil field through the coronagraph, and $\mathbf{p}_B \in \mathbb{R}^M$ is an experimentally-observed background distribution with flux rate $\lambda_B \in \mathbb{R}$ (Appendix B). For simplicity, the flux rates λ_0, λ_B

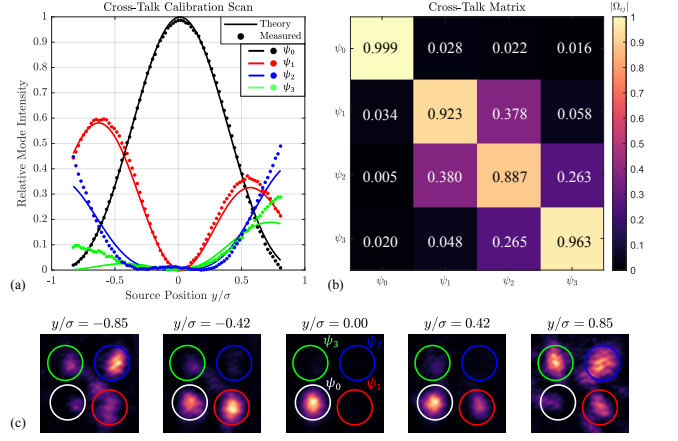


FIG. 4. (a) Cross-talk calibration data (dotted) of relative mode intensity in each channel as a function of off-axis source position. The relative intensities were measured at the sorting plane of the MPLC. Solid curves correspond to theoretically predicted mode intensities under a least-squares fit of the unitary cross-talk matrix to calibration data. (b) Magnitude of the entries in the cross-talk matrix. The relative power leakage from the fundamental mode into all other modes (square of column 1 entries) sums to $\sim 10^{-3}$, setting the limit of accessible star-planet contrasts for our experimental setup. (c) Measurements at the sorting plane with region segmentation for measuring energy in each mode.

are given in photons per integration period T . The action of the coronagraph on the incoming optical field appears in the post-nulling photon arrival probability,

$$\mathbf{q}(\vec{r}_0) = |\Psi \Omega C \Omega^\dagger \Psi^\dagger \psi_0(\vec{r}_0)|^2, \quad (2)$$

where the input field $\psi_0(\vec{r}_0)$ is a shifted version of the fundamental mode induced by illumination by a point source located at \vec{r}_0 . The $|\cdot|^2$ operation is applied element-wise to convert the field at each pixel to intensity. We have also introduced several system-dependent matrices: $\Psi \in \mathbb{C}^{M \times K}$ is a truncated change-of-basis matrix that transforms a field from its modal representation to its spatial representation, $C \in \mathbb{R}^{K \times K}$ is a diagonal nulling matrix which acts to reject the fundamental mode, and $\Omega \in \mathbb{C}^{K \times K}$ is the unitary cross-talk matrix of the mode sorter whose entries are determined from calibration measurements (Appendix C).

A synthetic measurement of a star-planet system $\mathbf{Y} = \mathbf{X}_s + \mathbf{X}_e$ is constructed by adding multiple measurement realizations of the artificial star and exoplanet illuminated independently such that $\mathbf{X}_s = \sum_{i=1}^{N_s} \mathbf{X}^{(i)}(\vec{0})$ and $\mathbf{X}_e = \mathbf{X}(\vec{r}_e)$ where \vec{r}_e is the position of the exoplanet. The choice of N_s sets the star-planet contrast. We employ this synthetic measurement scheme to circumvent interference effects that would arise if both star and exoplanet were illuminated simultaneously by the laser source in our setup. The synthetic measurement thus constitutes an approximation of measuring two incoherent point sources with unequal brightness. The complete measurement model is given by,

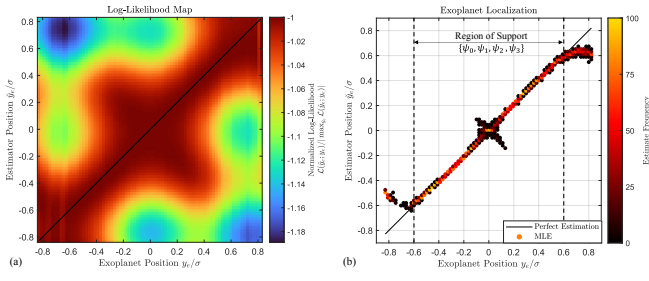


FIG. 5. **(a)** Map of the log-likelihood $\mathcal{L}(\check{y}_e; y_e)$ over sub-diffraction exoplanet locations. The peak likelihood ridgeline (dark red regions) nearly coincides with perfect localization (black diagonal). However certain regions near the optical axis and outside the support of the truncated mode basis exhibit weakly-peaked likelihoods indicating greater MLE uncertainty. **(b)** Scatter plot of the MLEs obtained at each ground truth position. The colorbar indicates the frequency/density with which each estimate was made. Some outliers were removed for visual clarity.

$$\mathbf{Y}(\vec{r}_e) \sim \text{Pois} \left(\Lambda_0 \mathbf{p}(\vec{r}_e) + \Lambda_B \mathbf{p}_B \right), \quad (3)$$

where $\Lambda_0 = N\lambda_0$, $\Lambda_B = N\lambda_B$, and $N = N_s + 1$ being the total number of measurement realizations. We define the photon distribution from the star-planet system as,

$$\mathbf{p}(\vec{r}_e) = (1 - b)\mathbf{q}(\vec{0}) + b\mathbf{q}(\vec{r}_e), \quad (4)$$

with $b = 1/N$ representing the relative brightness of the exoplanet. For our particular experimental setup we have integer constants $K = 4$, $M = 77^2$, and $N_s = 1000$.

III. RESULTS

A. Exoplanet Localization

In Figure 7, we compare simulated and experimental images of an artificial star-planet system captured with our coronagraph. For separations $|y_e| > 0.1\sigma$, where the signal-to-noise ratio (SNR) of the exoplanet exceeds ~ 1 , there are strong qualitative similarities between the simulated and experimental image intensity profiles, indicating that the exoplanet signal dominates over background noise. However, at separations below this threshold, where the vast majority exoplanet light is discarded with the fundamental mode, the noise in our experimental system becomes more prominent than the exoplanet signal. Additionally, we find that the asymmetry observed between images of the exoplanet positioned at equal distances above and below the optical axis ($\pm y_e$) emerges due to modal cross-talk.

For each exoplanet location $y_e \in \mathcal{Y}$, we compiled repeated synthetic measurements $\mathbf{Y}^{(i)}(y_e)$ for $i = 1, \dots, \ell$ (with $\ell = 100$)

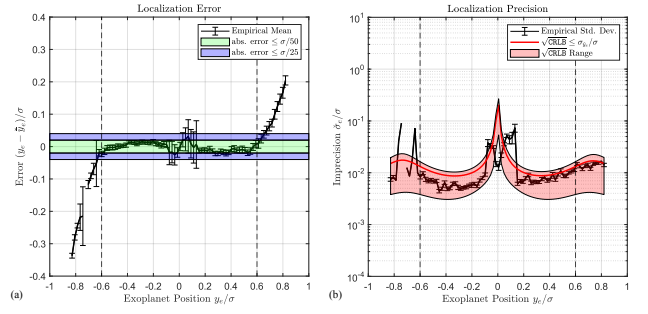


FIG. 6. **(a)** Mean empirical error of the exoplanet MLE as a function of the ground truth position (black curve). Green and blue shaded regions indicate star-planet separations where the localization error is below $\sigma/50$ and $\sigma/25$ respectively. **(b)** Statistical standard deviation of the MLE as a function of exoplanet position as compared to the Cramer-Rao lower bound (CRLB) for the measurement model of Equation 3. Uncertainty bars on the imprecision estimator were calculated using jackknife resampling [32]. Red shaded region indicates viable bounds of the CRLB given uncertainty in the experimental model parameters. In particular we show the upper and lower bounds of the CRLB associated with the left and right sides of FWHM, respectively, for λ_0 in Figure 10 (Appendix C).

with exposure time $T = 0.1\text{s}$. To localize the exoplanet we employ a maximum likelihood estimator (MLE),

$$\check{y}_e^{(i)}(y_e) = \underset{y'_e \in \mathcal{Y}}{\text{argmax}} \log P(\mathbf{Y}^{(i)}(y_e) | y'_e) \quad (5)$$

Figure 5(a) shows a map of the log-likelihood $\mathcal{L}(y_e; y'_e) = \log P(\mathbf{Y}(y_e) | y'_e)$ averaged over all experimental trials. The likelihood map exhibits a peak ridgeline (maximum likelihood) that corresponds almost exactly with the ground-truth position of the exoplanet, though exoplanet positions near the optical axis and outside of the modal region of support demonstrate greater estimator uncertainty (weakly-peaked likelihood). Figure 5b shows the MLEs obtained for all repeated measurements in the exoplanet translation scan. The estimator effectively localizes the exoplanet within the nominal region of support $|y_e| \leq .6\sigma$ of the truncated mode basis. Outside of this domain, the estimator experiences a bias due to the finite support of the truncated experimental mode set.

B. Statistical Performance Analysis

To quantify the performance of our coronagraph, we analyze the statistical error and imprecision of the MLE over repeated experimental trials. For a given, ground truth exoplanet position, we denote the mean and variance of the MLE to be $\bar{y}_e \equiv \mathbb{E}_{\mathbf{Y}|y_e}[\check{y}_e]$ and $\sigma_e^2 = \mathbb{V}_{\mathbf{Y}|y_e}[\check{y}_e]$ respectively. The unbiased empirical estimators of the MLE mean and variance are given by,

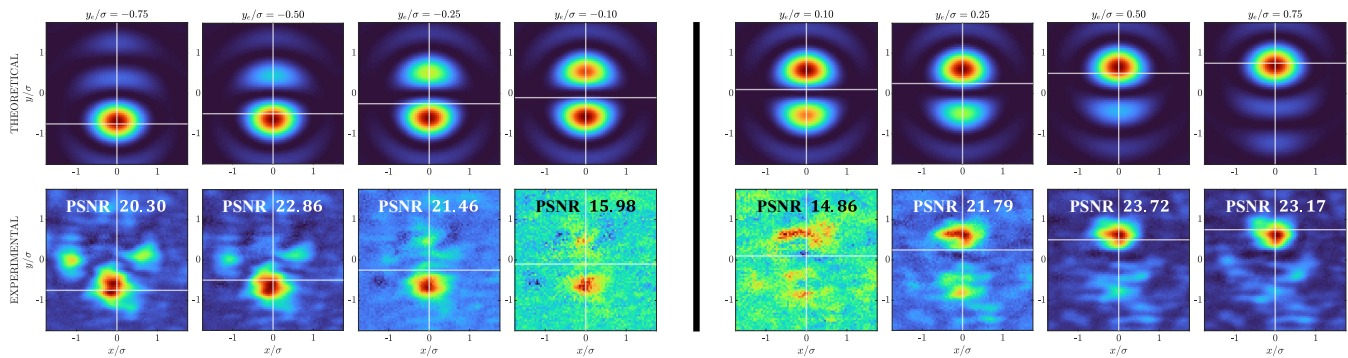


FIG. 7. A comparison between theoretically predicted and measured intensity distributions for different sub-diffraction star-planet separations under a 1000:1 star-planet contrast. Theoretical images were simulated for an idealized version of our experimental system without background or modal crosstalk. In each image, the ground truth location of the exoplanet is coincides with the white crosshairs. The experimental measurements are shown after subtraction of the background. Asymmetries in the experimental intensity distributions for equidistant off-axis $\pm y_e$ exoplanet locations stem from modal cross-talk shown in Figure 4.

$$\check{y}_e(y_e) \equiv \frac{1}{\ell} \sum_{i=1}^{\ell} \check{y}_e^{(i)}(y_e), \text{ and} \quad (6a)$$

$$\check{\sigma}_e^2(y_e) \equiv \frac{1}{\ell-1} \sum_{i=1}^{\ell} (\check{y}_e^{(i)}(y_e) - \check{y}_e(y_e))^2. \quad (6b)$$

Figure 6(a) shows the statistical error of the MLE over the complete domain of the exoplanet positional scan. In the subdomain $|y_e| \in [0.1, 0.6]\sigma$, the absolute error is $|\check{y}_e - y_e| < 0.02\sigma$ with an estimator imprecision $\check{\sigma}_{y_e} \approx 0.01$. In the subdomain $|y_e| \in [.01, .1]\sigma$, the absolute error is $|\check{y}_e - y_e| < 0.03\sigma$ with imprecision $< \check{\sigma}_{y_e} \approx 0.1$. Figure 6(b) shows the empirical imprecision of the MLE as a function of the exoplanet position. We find that this empirical imprecision curve corresponds with the classical Cramer-Rao Lower Bound (CRLB) computed for our experimental measurement model. When the exoplanet is near the optical axis, most of the photons its photons couple to the fundamental mode and are discarded. Thus, the majority of detected photons are supplied by the background, giving rise to a central spike in the imprecision. Additionally, two secondary peaks in imprecision appear at outside the region of support for the truncated mode basis.

IV. CONCLUSION

In review, we have experimentally developed a quantum-optimal direct imaging coronagraph using spatial mode (de)multiplexing. We demonstrate high-accuracy localization of an artificial exoplanet at sub-diffraction distances from its host star under 1000 : 1 star-planet brightness contrast. The performance of our experimental system at deeply sub-diffraction separations is fundamentally limited by a combination of detector dark noise, stray light, and modal cross-talk. At large star-planet separations our system performance is limited by the truncation of the mode basis, which may be

improved by extending the number of MPLC phase planes. Overall, we believe this work further substantiates the potential value of mode-sorting solutions for astronomical imaging tasks.

Looking forward, even-order coronagraphs may be implemented using similar mode filtering principles presented here. Such a coronagraph would temper photon shot noise induced by a star of finite extent [22]. Furthermore, extending functionality to broadband sources is necessary for analyzing the spectrum of the exoplanet. It is well-known that broadband sources introduce modal mismatch such that the cross-talk matrix becomes wavelength-dependent. For sub-diffraction exoplanets, the constraints on modal mismatch become more stringent [33, 34]. Interestingly, preliminary numerical work suggests that the MPLC method may be used to simultaneously sort spectral and spatial modes [35], providing a common solution for exoplanet spectroscopy and/or broadband nulling of the star.

V. ACKNOWLEDGEMENTS

ND acknowledges support from the National Science Foundation Graduate Research Fellowship under Grant No. DGE-2137419. IO and SG acknowledge that this research was supported by Raytheon and recognize the contributions of Jaime Bucay and Mark Meisner for their insights.

- [1] J. T. Wright and B. S. Gaudi, “Exoplanet detection methods,” (2012), [arXiv:1210.2471 \[astro-ph\]](#).
- [2] R. L. Akeson, X. Chen, D. Ciardi, M. Crane, J. Good, M. Harbut, E. Jackson, S. R. Kane, A. C. Laity, S. Leifer, M. Lynn, D. L. McElroy, M. Papin, P. Plavchan, S. V. Ramírez, R. Rey, K. von Braun, M. Wittman, M. Abajian, B. Ali, C. Beichman, A. Beekley, G. B. Berriman, S. Berukoff, G. Bryden, B. Chan, S. Groom, C. Lau, A. N. Payne, M. Regelson, M. Saucedo, M. Schmitz, J. Stauffer, P. Wyatt, and A. Zhang, “The nasa exoplanet archive: Data and tools for exoplanet research,” *Publications of the Astronomical Society of the Pacific* **125**, 989 (2013).
- [3] J. Schneider, C. Dedieu, P. Le Sidaner, R. Savalle, and I. Zolotukhin, “Defining and cataloging exoplanets: the exoplanet.eu database,” *Astronomy & Astrophysics* **532**, A79 (2011).
- [4] T. Currie, B. Biller, A.-M. Lagrange, C. Marois, O. Guyon, E. Nielsen, M. Bonnefoy, and R. D. Rosa, “Direct imaging and spectroscopy of extrasolar planets,” (2023), [arXiv:2205.05696 \[astro-ph.EP\]](#).
- [5] W. A. Traub and B. R. Oppenheimer, *Direct imaging of exoplanets* (University of Arizona Press, Tucson, 2010).
- [6] S. Seager and D. Deming, “Exoplanet atmospheres,” *Annual Review of Astronomy and Astrophysics* **48**, 631–672 (2010).
- [7] B. A. Biller and M. Bonnefoy, “Exoplanet atmosphere measurements from direct imaging,” in *Handbook of Exoplanets*, edited by H. J. Deeg and J. A. Belmonte (Springer International Publishing, Cham, 2018) pp. 2107–2135.
- [8] B. Biller, “Detecting and characterizing exoplanets with direct imaging: past, present, and future,” *Proceedings of the International Astronomical Union* **8**, 1–11 (2013).
- [9] G. Foo, D. M. Palacios, and G. A. Swartzlander, “Optical vortex coronagraph,” *Opt. Lett.* **30**, 3308–3310 (2005).
- [10] E. Mari, F. Tamburini, G. A. Swartzlander, A. Bianchini, C. Barbieri, F. Romanato, and B. Thidé, “Sub-rayleigh optical vortex coronagraphy,” *Opt. Express* **20**, 2445–2451 (2012).
- [11] O. Guyon, F. Martinache, R. Belikov, and R. Soummer, “High performance piala coronagraphy with complex amplitude focal plane masks,” *The Astrophysical Journal Supplement Series* **190**, 220 (2010).
- [12] C. Aime, R. Soummer, and A. Ferrari, “Total coronagraphic extinction of rectangular apertures using linear prolate apodizations,” *Astronomy & Astrophysics* **389**, 334–344 (2002).
- [13] R. Soummer, C. Aimé, and P. Falloon, “Stellar coronagraphy with prolate apodized circular apertures,” *Astronomy & Astrophysics* **397**, 1161–1172 (2003).
- [14] R. Soummer, “Apodized pupil lyot coronagraphs for arbitrary telescope apertures,” *The Astrophysical Journal* **618**, L161 (2004).
- [15] A. Zurlo, “Direct imaging of exoplanets,” (2024), [arXiv:2404.05797 \[astro-ph.EP\]](#).
- [16] O. Guyon, E. A. Pluzhnik, M. J. Kuchner, B. Collins, and S. T. Ridgway, “Theoretical limits on extrasolar terrestrial planet detection with coronagraphs,” *The Astrophysical Journal Supplement Series* **167**, 81 (2006).
- [17] N. Deshler, S. Haffert, and A. Ashok, “Achieving quantum limits of exoplanet detection and localization,” (2024), [arXiv:2403.17988 \[quant-ph\]](#).
- [18] M. Tsang, R. Nair, and X.-M. Lu, “Quantum theory of super-resolution for two incoherent optical point sources,” *Phys. Rev. X* **6**, 031033 (2016).
- [19] M. Tsang, “Resolving starlight: a quantum perspective,” *Contemporary Physics* **60**, 279–298 (2019).
- [20] K. K. Lee, C. N. Gagatsos, S. Guha, and A. Ashok, “Quantum-inspired multi-parameter adaptive bayesian estimation for sensing and imaging,” *IEEE Journal of Selected Topics in Signal Processing* **17**, 491–501 (2023).
- [21] S. Prasad, “Quantum limited super-resolution of an unequal-brightness source pair in three dimensions,” *Physica Scripta* **95**, 054004 (2020).
- [22] R. Belikov, D. Sirbu, J. B. Jewell, O. Guyon, and C. C. Stark, “Theoretical performance limits for coronagraphs on obstructed and unobstructed apertures: how much can current designs be improved?” in *Techniques and Instrumentation for Detection of Exoplanets X*, Society of Photo-Optical Instrumentation Engineers (SPIE) Conference Series, Vol. 11823 (2021) p. 118230W.
- [23] A.-M. Lagrange, F. Philipot, P. Rubini, N. Meunier, F. Kiefer, P. Kervella, P. Delorme, and H. Beust, “Radial distribution of giant exoplanets at solar system scales,” *Astronomy & Astrophysics* **677**, A71 (2023).
- [24] R. B. Fernandes, G. D. Mulders, I. Pascucci, C. Mordasini, and A. Emsenhuber, “Hints for a turnover at the snow line in the giant planet occurrence rate,” *The Astrophysical Journal* **874**, 81 (2019).
- [25] J. Chen and D. Kipping, “Probabilistic forecasting of the masses and radii of other worlds,” *The Astrophysical Journal* **834**, 17 (2016).
- [26] B. Ning, A. Wolfgang, and S. Ghosh, “Predicting exoplanet masses and radii: A nonparametric approach,” *The Astrophysical Journal* **869**, 5 (2018).
- [27] J. Carpenter, N. K. Fontaine, B. R. M. Norris, and S. Leon-Saval, “Spatial mode sorter coronagraphs,” in *CLEO PR 2020* (Optica Publishing Group, 2020).
- [28] N. K. Fontaine, R. Ryf, H. Chen, D. T. Neilson, K. Kim, and J. Carpenter, “Laguerre-gaussian mode sorter,” *Nature Communications* **10** (2019), [10.1038/s41467-019-09840-4](#).
- [29] G. Labroille, B. Denolle, P. Jian, P. Genevaux, N. Treps, and J.-F. Morizur, “Efficient and mode selective spatial mode multiplexer based on multi-plane light conversion,” *Opt. Express* **22**, 15599–15607 (2014).
- [30] J. Řehaček, Z. Hradil, B. Stoklasa, M. Paúr, J. Grover, A. Krzic, and L. L. Sánchez-Soto, “Multiparameter quantum metrology of incoherent point sources: Towards realistic superresolution,” *Phys. Rev. A* **96**, 062107 (2017).
- [31] I. Ozer, M. R. Grace, and S. Guha, “Reconfigurable spatial-mode sorter for super-resolution imaging,” in *2022 Conference on Lasers and Electro-Optics (CLEO)* (IEEE, 2022) pp. 1–2.
- [32] C.-F. J. Wu, “Jackknife, bootstrap and other resampling methods in regression analysis,” *the Annals of Statistics* **14**, 1261–1295 (1986).
- [33] S. Prasad, “Quantum limited source localization and pair super-resolution in two dimensions under finite-emission bandwidth,” *Phys. Rev. A* **102**, 033726 (2020).
- [34] M. R. Grace, “Quantum limits and optimal receivers for passive sub-diffraction imaging,” (2022).
- [35] Y. Zhang, H. Wen, A. Fardoost, S. Fan, N. K. Fontaine, H. Chen, P. L. Likamwa, and G. Li, “Simultaneous sorting of wavelengths and spatial modes using multi-plane light conversion,” (2020), [arXiv:2010.04859 \[physics.optics\]](#).

- [36] G. ming Dai, "Zernike aberration coefficients transformed to and from fourier series coefficients for wavefront representation," *Opt. Lett.* **31**, 501–503 (2006).
- [37] T. Abrudan, J. Eriksson, and V. Koivunen, "Optimization under unitary matrix constraint using approximate matrix exponential," in [39th Asilomar Conference on Signals, Systems and Computers](#) (2005) pp. 242–246.
- [38] A. C. Aitken, "Iv.—on least squares and linear combination of observations," *Proceedings of the Royal Society of Edinburgh* **55**, 42–48 (1936).

Appendix A: Fourier-Zernike Modes

For an imaging system with circular pupil of radius R , focal length f , and operating wavelength λ , let (X_a, Y_a) and (X_b, Y_b) denote the coordinate space of the pupil plane and focal plane respectively. We define the dimensionless pupil plane and focal plane coordinate vectors,

$$\vec{u} \equiv \frac{1}{R}(X_a, Y_a) \quad (\text{A1a})$$

$$\vec{r} \equiv \frac{R}{\lambda f}(X_b, Y_b) \quad (\text{A1b})$$

The Zernike modes $\tilde{\psi}_{nm}(\vec{u})$ constitute a PSF-matched basis over a circular pupil. In polar coordinates, they are given by,

$$\tilde{\psi}_{nm}(u, \theta) \equiv R_{nm}(u)\Theta_m(\theta)\text{circ}(u) \quad (\text{A2a})$$

$$R_{nm}(u) \equiv \sum_{j=0}^{(n-|m|)/2} \frac{(-1)^j \sqrt{n+1} (n-j)!}{j! [(n+m)/2 - j]! [(n-m)/2 - j]!} u^{n-2j} \quad (\text{A2b})$$

$$\Theta_m(\theta) \equiv \begin{cases} \sqrt{2} \cos(|m|\theta) & (m > 0) \\ 1 & (m = 0) \\ \sqrt{2} \sin(|m|\theta) & (m < 0) \end{cases} \quad (\text{A2c})$$

$$\text{circ}(u) \equiv \begin{cases} 1, & u \leq 1 \\ 0, & u > 1 \end{cases} \quad (\text{A2d})$$

where the radial index range is $n = 0, 1, 2, \dots, \infty$. The angular index range for a given radial index is $m \in S_n = \{-n, -n+2, \dots, n-2, n\}$. These modes are defined to satisfy the orthonormality condition,

$$\int \tilde{\psi}_{nm}^*(u, \theta) \tilde{\psi}_{n'm'}(u, \theta) u du d\theta = \delta_{nn'} \delta_{mm'}$$

The Fourier transform of the Zernike modes over the pupil are found in [36] to be,

$$\psi_{nm}(r, \phi) = i^{n+2|m|} \sqrt{n+1} \frac{J_{n+1}(2\pi r)}{\sqrt{\pi r}} \Theta_m(\phi) \quad (\text{A3})$$

which we refer to as the 'Fourier-Zernike' modes throughout the main text. In this work, we sort the truncated mode basis $\{\psi_0, \psi_1, \psi_2, \psi_3\}$ corresponding to modes $\{\psi_{00}, \psi_{1,-1}, \psi_{2,0}, \psi_{2,2}\}$. The squared magnitude of these modes is shown in Figure 2c.

Appendix B: Measurement Model

Here we expand on the single-shot measurement model of Equation 3. The post-nulling optical intensity distribution on

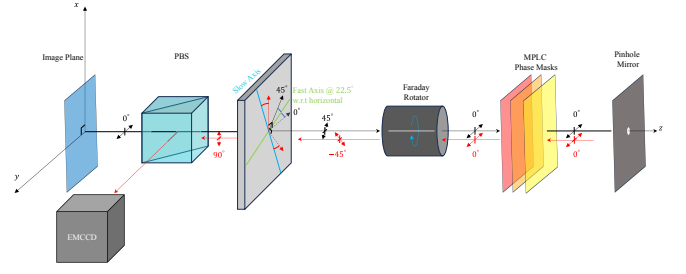


FIG. 8. Unfolded beam path illustrating polarization control for path splitting of forward (black arrows) and backward (red arrows) propagating beams. Through this manipulation we implement the design of Figure 2 using a single mode sorter.

the detector is modeled as,

$$\mathbf{q}(\vec{r}_0) = |\Psi \Omega C \Omega^\dagger \Psi^\dagger \psi_0(\vec{r}_0)|^2 \quad (\text{B1})$$

which provides a matrix description of forward propagating the optical field through the MPLC, nulling the fundamental mode, back-propagating the field to an image plane, and measuring the intensity on a detector array. Here, $\psi_0(\vec{r}_0) = \text{vec}[\psi(\vec{r} - \vec{r}_0)]$ is the vectorized form of the shifted PSF satisfying $\psi_0(\vec{r}_0)^\dagger \psi_0(\vec{r}_0) = 1$. Ψ is the truncated change-of-basis matrix for which the columns are the vectorized Fourier-Zernike modes $\psi_k = \text{vec}[\psi_k(\vec{r})]$

$$\Psi = \begin{bmatrix} | & & | \\ \psi_0 & \cdots & \psi_{K-1} \\ | & & | \end{bmatrix} \quad (\text{B2})$$

satisfying the orthonormality condition $\Psi^\dagger \Psi = I_K$ where I_K is the identity on \mathbb{C}^K . The coronagraph matrix is given by,

$$C = \begin{bmatrix} 0 & \mathbf{0}^T \\ \mathbf{0} & I_{K-1} \end{bmatrix} \quad (\text{B3})$$

which serves to null the fundamental mode (in the absence of cross-talk). While we treat the optical field as a scalar quantity (as the field is always in a definite linear polarization state throughout our experiment), details on the experimental polarization manipulation for path splitting are illustrated in Figure 8.

Appendix C: Calibration

This section addresses our procedures for characterizing all system-level parameters involved in the measurement model:

$$\{\Omega, \lambda_D, \lambda_0, \mathbf{s}\}$$

1. Cross-Talk Matrix Ω

Figure 4 shows calibration measurements made for characterizing modal cross-talk through the MPLC. We estimate the cross-talk matrix from these calibration measurements by optimizing a least-squares objective function $\mathcal{F}(\Omega)$ under the constraint that Ω be unitary,

$$\check{\Omega} = \underset{\Omega: \Omega^\dagger \Omega = I_K}{\operatorname{argmin}} \underbrace{\|M - (\Omega Z) \odot (\Omega Z)^*\|_F^2}_{\mathcal{F}(\Omega)} \quad (\text{C1})$$

where $\|\cdot\|_F$ is the Frobenius-norm and \odot is the Hadamard element-wise product. In formulating this optimization problem, we define the following terms:

- $Z \in \mathbb{R}^{K \times P}$: Zernike expansion coefficients for each off-axis source location.
- $M \in \mathbb{R}^{K \times P}$: Measurements of intensity in each mode channel.
- $\Gamma_\Omega = \nabla_{\Omega} \mathcal{F}$: Gradient of the objective function with respect to the cross-talk matrix.
- $G(\Omega) = \Gamma_\Omega \Omega^\dagger - \Omega \Gamma_\Omega^\dagger$: Riemannian gradient of the objective function (Hermitian).

The number of off-axis point-source locations measured is $P = |\mathcal{Y}|$. We solve this optimization using the constrained gradient optimization algorithm detailed in [37]. The algorithm is briefly summarized as follows. Instantiate $\Omega_0 = I$ with learning rate $\mu > 0$. Then, at iteration t , we update the cross-talk matrix as

$$\Omega_{t+1} = \expm(-\mu G_t) \Omega_t \quad (\text{C2})$$

where $G_t = G(\Omega_t)$. The iterations are performed until convergence. In Figure 4a, we show the measured mode intensity data alongside the theoretical mode intensities after applying the best-fit cross-talk matrix shown in 4b.

2. Dark Noise Rate λ_D and Structured Background \mathbf{s}

The background contribution term employed in our single-shot measurement model arises from a combination of undesired stray light reflections and the dark noise rate of the pixels in the camera. We thus decompose the background into two terms as,

$$\lambda_B \mathbf{p}_B = \mathbf{s} + \lambda_D \mathbf{1} \quad (\text{C3})$$

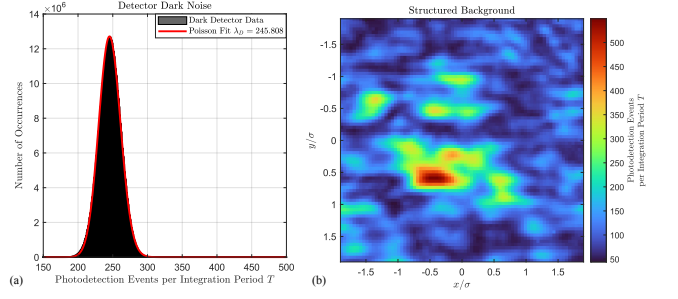


FIG. 9. (a) Poisson fit to detector dark-noise histogram. The dark rate of the detector was found to be $\lambda_D = 246$ [photons $\cdot T^{-1}$] per pixel. (b) Structured background profile \mathbf{s} induced by stray light and undesired reflections in the experimental setup.

where $\mathbf{s} \in \mathbb{R}^M$ is a structured background rate observed across our experimental measurements, and $\lambda_D \in \mathbb{R}$ is the spatially-uniform dark click rate of each pixel operating a room temperature. Furthermore, $\mathbf{1} \in \mathbb{R}^M$ is a vector of ones, and we have impose the constraint $\mathbf{1}^\top \mathbf{p}_B = 1$ such that \mathbf{p}_B is a discrete probability distribution. Figure 9 shows calibration data for estimating the dark noise rate λ_D and structured background rate \mathbf{s} of Equation 1. An estimate of the dark noise rate $\check{\lambda}_D = 246$ [photons/ T] was found by fitting a Poisson distribution to a histogram of photon counts recorded by our camera operating in a dark environment at room temperature. The structured background rate was estimated by averaging $n = 10^3$ images of the an on-axis source as viewed through the coronagraph,

$$\check{\mathbf{s}} = \frac{1}{n} \sum_{i=1}^n [\mathbf{X}^{(i)}(\vec{0}) - \lambda_D \mathbf{1}] \quad (\text{C4})$$

where we have assumed that the photons arriving at the detector due to imperfect nulling of the fundamental mode (i.e. modal cross-talk) are negligible compared to the dark noise rate $\lambda_0 \mathbf{q}(\vec{0}) \ll \lambda_D$.

3. Signal Photon Rate λ_0

The mean photon rate entering the pupil from the star-planet scene is approximated using the Best Linear Unbiased Estimator (BLUE) [38]. Let the random variable $Y_j^{(i)}(\vec{r}_e)$ represent the photons collected in the j^{th} pixel of the i^{th} measurement for a given exoplanet location \vec{r}_e . In accordance with equation 3, each pixel follows distribution

$$Y_j^{(i)}(\vec{r}_e) \sim \text{Pois} \left(\Lambda_0 p_j(\vec{r}_e) + \Lambda_B p_{B_j} \right)$$

which we approximate as a non-random term linear in Λ_0 with zero-mean additive Gaussian noise,

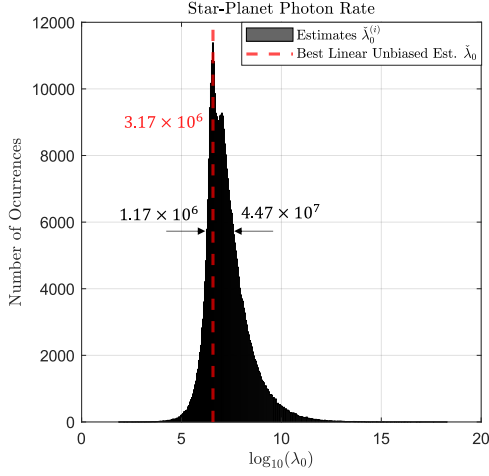


FIG. 10. Histogram over estimates of the scene photon emission rate λ_0 from which we compute the best linear unbiased estimator (dashed red) $\check{\lambda}_0 = 3.17 \times 10^6$ [Photons $\cdot T^{-1}$]. The edges of the FWHM are used in Figure 6 to determine the range of Cramer-Rao Bounds associated with our experiment.

$$Y_j^{(i)}(\vec{r}_e) = \Lambda_0 p_j(\vec{r}_e) + \Lambda_B p_{B_j} + \varepsilon_j \quad (C5)$$

$$\varepsilon_j(\Lambda_0, \vec{r}_e) \sim \mathcal{N}(0, \Lambda_0 p_j(\vec{r}_e) + \Lambda_B p_{B_j}) \quad (C6)$$

Defining the residuals,

$$r_j^{(i)}(\Lambda_0, \vec{r}_e) = Y_j^{(i)}(\vec{r}_e) - \Lambda_0 p_j(\vec{r}_e) - \Lambda_B p_{B_j}$$

the BLUE is found by optimizing the sum of squared residuals weighted by the variance of the photon arrivals in each pixel

$$\check{\Lambda}_0 = \operatorname{argmax}_{\Lambda_0} \sum_{y_e \in \mathcal{D}} \sum_{i=1}^{\ell} \sum_{j=1}^M \frac{(r_j^{(i)}(\Lambda_0, y_e))^2}{\mathbb{V}[\varepsilon_j(\Lambda_0, y_e)]}. \quad (C7)$$

We numerically solve this optimization problem over the entire collected data set and estimate the mean photon rate entering the pupil from a single point source to be $\check{\lambda}_0 = \check{\Lambda}_0/N = 3.17 \times 10^6$ [photons/T].

4. Throughput and Bias-Scaling

Figure 11 shows the experimental coronagraph throughput as a function of the scanned source position. Comparing the measured throughput to the theoretical throughput curve of our system revealed a scaling c and bias a between the true source displacements y_e relative to the diffraction limit and the displacements computed from our system specifications

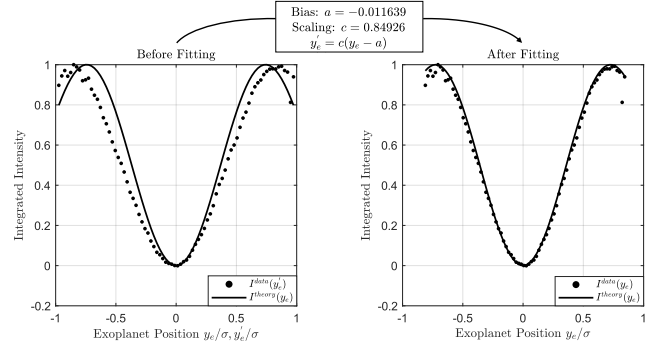


FIG. 11. Alignment and magnification discrepancies in 4f system are accounted for by fitting the experimental throughput to theoretically-predicted values.

$y_e' = c(y_e - a)$. The scaling and bias terms arise from experimental error in magnification and alignment of the optical axis. Accounting for these discrepancies revealed the true range $y_e/\sigma \in [-.85, .85]$ over which we scanned our point source.

Appendix D: Function Vectorization

Let $\Delta x, \Delta y$ be the horizontal and vertical pixel pitch dimensions for specific camera, and let $\{(x_i, y_i)\}_{i=1}^M$ be the set of points corresponding to the center of each pixel. The $\operatorname{vec}(\cdot)$ operation takes a well-behaved function $f(x, y)$ over the plane and converts it to a column vector \mathbf{f} whose entries are given by,

$$\mathbf{f}_i = \int_{x_i - \Delta x/2}^{x_i + \Delta x/2} \int_{y_i - \Delta y/2}^{y_i + \Delta y/2} f(x, y) dx dy \quad (D1)$$

Appendix E: Numerical Comparisons to Other Coronagraphs

As points of comparison, we numerically evaluate the performance of experimental coronagraph against the PI-AACMC, Vortex (charge-2) coronagraph, and the Perfect coronagraph. The Perfect coronagraph is the idealized version of our experimental implementation in the absence of mode truncation or cross-talk. We assign the same background illumination profile espoused in our experiment $\Lambda_B \mathbf{p}_B$ to the measurement model of each coronagraph. Then, the distinguishing factor between coronagraphs manifests in the term $\Lambda_0 \mathbf{p}(\vec{r}_e)$ which now depends on singular-value decomposition of the field transformation performed by a given coronagraph,

$$\mathbf{q}(\vec{r}_0) = |U \Sigma V^\dagger \boldsymbol{\psi}(\vec{r}_0)|^2 \quad (E1)$$

where $U, V \in \mathbb{C}^{M \times M}$ are unitary matrices and $\Sigma \in \mathbb{R}^{M \times M}$

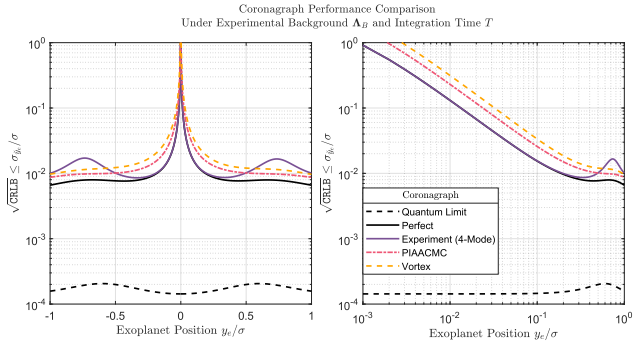


FIG. 12. Comparison of the Cramer-Rao Lower Bounds on imprecision of an unbiased estimator of the exoplanet position for different coronagraphs operating under the same empirical background model found in our experimental system. The quantum limit curve (black dashed) is for a shot-noise-limited situation without any background contribution.

is a diagonal matrix of singular values. Figure 12 shows the Cramer-Rao lower bounds associated with each coronagraph. We see that the idealized version of our experimental setup (Experiment 4-Mode) outperforms both the PIAACMC and Vortex coronagraph for over sub-diffraction exoplanet locations in the range $|y_e| \leq 0.4\sigma$ which corresponds to where the CFI of the truncated mode basis begins to depart from the QFI limit as shown in Figure 3b.